

# Characterization and Impact of Large-Signal Dielectric Properties in MnZn Ferrites

Thomas Guillod\*, William V. R. Roberts<sup>†</sup>, and Charles R. Sullivan\*

\*Dartmouth College, Hanover NH, United States

<sup>†</sup>Princeton University, Princeton NJ, United States

**Abstract**—A time-varying magnetic flux in a magnetic core generates an induced electric field (Faraday’s law of induction). This implies that the dielectric properties of ferrites play a critical role in the behavior of large magnetic cores, affecting the onset and severity of dimensional resonances and magnetic skin effect. Therefore, this paper analyzes small-signal and large-signal dielectric measurement techniques for power ferrites. The dielectric response of the “EPCOS TDK N87” MnZn ferrite is measured with respect to frequency, temperature, and amplitude. It is found that the dielectric properties are only slightly nonlinear. Finally, the impact of the dielectric properties on the wavelength, penetration depth, and total losses is computed with large-signal models. The dimensional effects can lead to a significant increase of the losses (up to 100 %).

**Index Terms**—Magnetic materials, ferrites, magnetic losses, dielectric losses, eddy currents, permittivity, modeling, electromagnetic coupling, dimensional resonance.

## I. INTRODUCTION

Soft-magnetic ferrites feature low losses over a wide frequency range and, therefore, are extensively used in power magnetics. The magnetic properties of ferrites are known to be extremely nonlinear and have been and are still the subject of extensive research [1]–[5]. However, applying a time-varying magnetic flux to a magnetic core also induces an electric field in the material, as shown in Fig. 1 [6], [7]. Hence, the dielectric properties of ferrites also influence the behavior and limit the performance of such materials [8]–[10]. At low frequencies, the eddy-currents do not affect the magnetic flux distribution and the analysis of the magnetic and dielectric effects can be decoupled. At high frequencies, the electric and magnetic effects are coupled and, therefore, the wave equation should be considered. This is particularly critical in MnZn ferrites because they combine large permeability ( $\mu_r \in [500, 5000]$ ) and extreme permittivity ( $\varepsilon_r \in [10^4, 10^6]$ ) [11], [12]. This implies that the wave propagation speed is several orders of magnitude slower than in vacuum, making these materials subject to wave propagation and skin effect at relatively low frequencies (below 1 MHz) [9], [13].

State-of-the-art characterization of the dielectric properties of ferrites is done with small-signal excitations [10]–[12]. The conduction mechanism between the ferrite grains is known to be impacted by non-linear tunneling charge transport [8], [14], indicating that small-signal models might underestimate the impact of the dimensional effects. However, to the knowledge of the authors, a comprehensive study of the large-signal dielectric

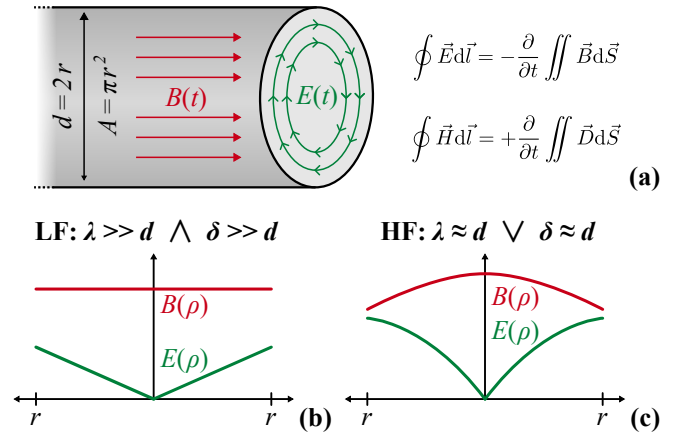


Fig. 1. (a) Induced electric field produced by a time-varying magnetic flux in a core with a circular cross-section. (b) Magnetic flux density and electric field patterns at low frequencies (the induced current is not impacting the flux distribution). (c) Magnetic flux density and electric field patterns at high frequencies (the induced current is impacting the flux distribution).

properties of ferrite materials (including capacitive and resistive effects) has never been conducted. Therefore, the goal of this paper is to characterize the large-signal dielectric response and assess the dimensional effects with large-signal models.

This paper is organized as follows. Section II characterizes the small-signal and large-signal dielectric properties of “EPCOS TDK N87” MnZn ferrites. The test fixture and the reproducibility of the measurements are discussed in detail. Section III analyzes the impact of the large-signal properties on the wavelength, penetration depth, and loss density using quasi-static and full wave models. The datasets and the source code are openly available [15], [16].

## II. DIELECTRIC CHARACTERIZATION OF MNZN FERRITES

The measurements of the dielectric properties are difficult in a magnetic circuit because the magnetic properties will typically dominate the material response. Hence, the dielectric properties are measured with a parallel-plate capacitor with a ferrite dielectric [7], [12]. If the electrode area is small, the dimensional effects are negligible and a homogeneous field distribution is obtained [12].

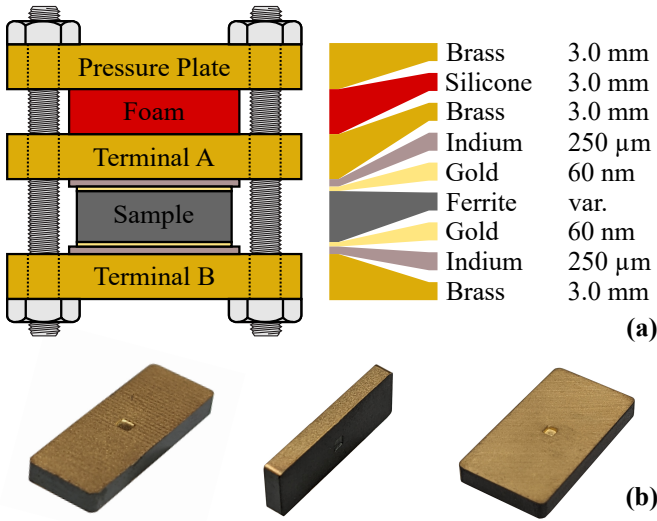


Fig. 2. (a) Test fixture for contacting a ferrite sample and creating a plate capacitor. (b) Ferrite samples with gold metallization.

### A. Measurement Setup

Creating the electrodes of a ferrite plate capacitor is a critical task as ferrites are not solderable and exhibit low electrical conductivities. Pressure contacts are not an option as mechanical stress changes the electrical properties of ferrites [12]. Typically, the electrodes are created with a carbon or silver coating of the surfaces [12]. However, it has been found that silver contacts (colloidal silver [17] and silver epoxy [18]) are not reliable and/or reproducible. Despite the low bulk conductivity of these materials, the interface resistance between the silver and the ferrite is not negligible. Moreover, the interface properties are strongly humidity-dependent and voltage-dependent.

For this reason, the test fixture depicted in Fig. 2(a) is used. In a first step, the ferrite electrodes are metallized with a 60 nm gold coating (using a “Hummer 6.2” sputter coater) [19]. During the sputtering, the side surfaces are protected with polyimide tape. The sputtering ensures a homogeneous metallization of the ferrite at the microscopic scale (see Fig. 2(b)). Due to the ferrite production process (sintering and firing), the sample surfaces typically exhibit large mechanical tolerances and mechanically processing the surfaces might alter the electrical properties [20]. Therefore, the gold-coated ferrite sample is contacted between the brass electrodes using a 250  $\mu\text{m}$  indium foil as an interface material. Indium, as a malleable metal, ensures consistent electrical and thermal contacts even if the electrode surfaces are not perfectly planar. Finally, the brass plates are pressed together with screws, using a high-temperature silicone foam to limit the applied mechanical pressure [12].

The electrical properties of ferrites are dependent on the humidity [21]. In order to obtain reproducible measurements, the following conditioning of the samples is applied. First, the samples are mounted in the test fixture and cured for three hours at 140 °C. Afterward, the complete test fixture is dried at

25 °C during twenty hours in a dry chamber (relative humidity below 8 %). Finally, the test fixture is placed in dielectric oil for the measurements. The oil prevents the diffusion of humidity into the sample during the measurements. Moreover, the oil is used, together with a magnetic hot plate stirrer, to control the temperature of the sample.

In this paper, “EPCOS TDK N87” rectangular samples (“I14/1.5/5”) are considered [22]. If not specified otherwise, the metallized electrode area is  $14.0 \text{ mm} \times 1.5 \text{ mm} = 21 \text{ mm}^2$  and the electrode distance is 5.0 mm.

### B. Small-Signal Properties

The small-signal impedance is measured with an “Agilent 4294A” precision impedance analyzer for different temperatures and frequencies [23]. The impedance of the test fixture terminations is compensated during the instrument calibration. The peak electric field is maintained below 0.05 V/mm. From the measured impedance, the complex relative permittivity can be extracted as

$$Z = \frac{1}{j2\pi f \epsilon_0 \epsilon_r \frac{A}{d}} \implies \epsilon_r = \frac{1}{j2\pi f \epsilon_0 Z \frac{A}{d}}, \quad (1)$$

where  $f$  is the frequency,  $A$  the sample area,  $d$  the sample thickness, and  $Z$  the measured impedance. Alternatively, the material properties can be represented by a real permittivity and an equivalent conductivity:

$$\epsilon_r = \epsilon'_r - j\epsilon''_r = \epsilon'_r - j\frac{\sigma}{2\pi f \epsilon_0}. \quad (2)$$

Note that the imaginary permittivity and the equivalent conductivity are two ways to represent the same losses, not measurements of independent additive loss effects. The losses linked with the equivalent conductivity as often referred as eddy-current losses. The real permittivity and the equivalent conductivity are directly linked to a parallel (resistive-capacitive) equivalent circuit [5]:

$$Z = \frac{1}{j2\pi f \epsilon_0 \epsilon_r \frac{A}{d}} = \frac{1}{j2\pi f \epsilon_0 \epsilon'_r \frac{A}{d} + \sigma \frac{A}{d}}. \quad (3)$$

Fig. 3 depicts the obtained complex permittivity and equivalent conductivity. At low frequencies, the imaginary permittivity is much larger than the real permittivity and the equivalent conductivity is nearly constant, indicating that the sample has a resistive behavior. At high frequencies, the sample becomes capacitive, which is explained by the drop of the imaginary permittivity. However, ferrites are extremely lossy dielectrics as the material quality factor remains below 4.0 over the measured frequency and temperature ranges. Due to the strong frequency dependence of the imaginary permittivity, it is more convenient to use the equivalent conductivity to describe the material losses [5]. Moreover, the real permittivity and the equivalent conductivity are directly linked to a simple parallel equivalent circuit (see (3)). The equivalent conductivity increases with respect to both the frequency and the temperature [11], [12].

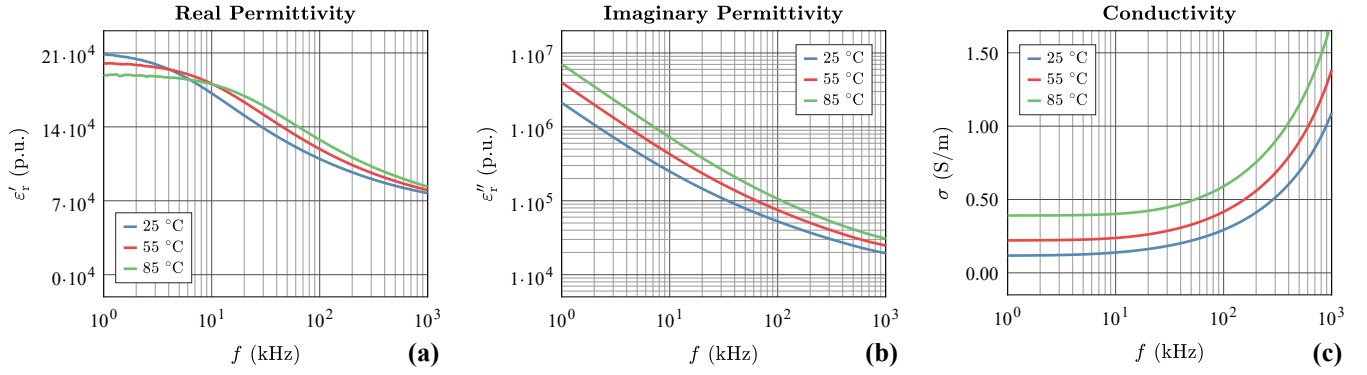


Fig. 3. (a) Real part of the complex permittivity, (b) imaginary part of the complex permittivity, and (c) equivalent conductivity. The measurements are conducted with “EPCOS TDK N87”. The peak electric field is maintained below 0.05 V/mm.

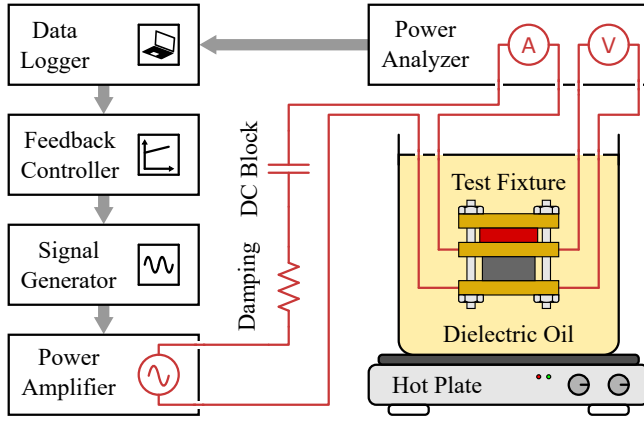


Fig. 4. Large-signal measurement setup using a power amplifier and a power analyzer. The electrical connections are highlighted in red.

In a magnetic circuit, the excitation is electric field (and not current density) driven (see Fig. 1). Therefore, the dielectric losses increase with the frequency and temperature.

### C. Large-Signal Properties

For large-signal measurements, a power amplifier is used to generate the sinusoidal excitation, as shown in Fig. 4. The voltage and current are measured with a “Voltech PM6000” precision power analyzer [24]. The test fixture is connected using a four-wire measurement method. The amplifier gain is adjusted by a feedback controller in order to match the desired electric field peak value.

From the measured voltage and current waveforms, the electric field, the current density, and the displacement field can be extracted as

$$E(t) = \frac{V(t)}{d}, \quad (4)$$

$$J(t) = \frac{\partial D(t)}{\partial t} = \frac{i(t)}{A}, \quad (5)$$

where  $A$  the sample area and  $d$  the sample thickness. Fig. 5(a) shows the dielectric hysteresis cycles for different amplitudes. It can be seen that the peak-to-peak permittivity is almost

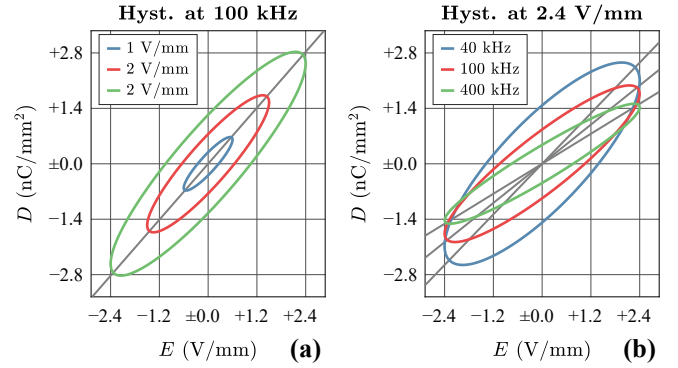


Fig. 5. (a) Large-signal dielectric hysteresis at 100 kHz. (b) Large-signal dielectric hysteresis at 2.4 V/mm. The amplitude permittivity is highlighted in gray. The measurements are conducted with “EPCOS TDK N87” at 25 °C.

independent of the amplitude. Fig. 5(b) depicts the cycles for different frequencies. Both the real and imaginary parts of the permittivity drop with increasing frequency, as already observed with small-signal measurements (see Fig. 3). It is interesting to observe that the losses per cycle (area enclosed by the hysteresis curve) decrease with frequency. However, the average losses (losses per cycle multiplied by the frequency) still increase with frequency.

The shape of the hysteresis loops is roughly elliptical which means the material behavior can be approximated by locally linearized parameters. The material parameters are linearized in the frequency domain with respect to the complex power density:

$$S_{\text{sum}} = \frac{1}{2} \sum_i \hat{E}_i \hat{J}_i^*, \quad (6)$$

$$E_{\text{rms}} = \sqrt{\frac{1}{2} \sum_i \hat{E}_i \hat{E}_i^*}, \quad (7)$$

$$\epsilon_r = \epsilon'_r - j \frac{\sigma}{2\pi f \epsilon_0} = \frac{S_{\text{sum}}^*}{j 2\pi f \epsilon_0 E_{\text{rms}}^2}, \quad (8)$$

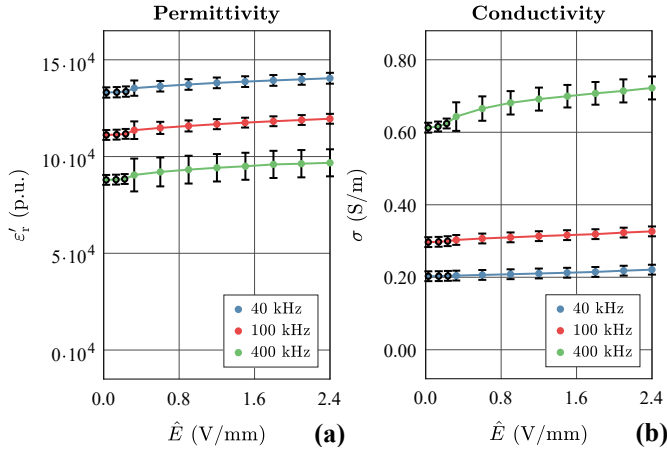


Fig. 6. (a) Real part of the complex permittivity and (b) equivalent conductivity. The measurements are conducted with “EPCOS TDK N87” at 25 °C. The points with an amplitude below 0.25 V/mm are measured with an impedance analyzer (circled in black). The large-signal measurements are taken with a power amplifier and a power analyzer.

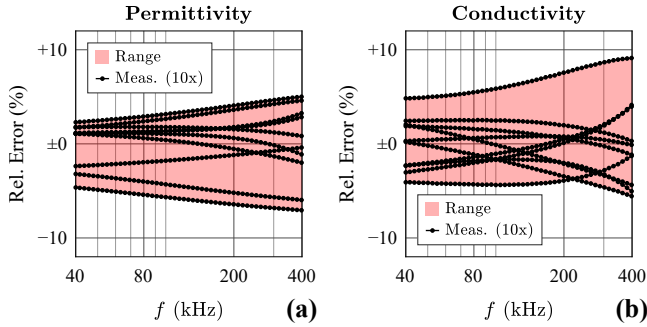


Fig. 7. Sample to sample variation for the (a) real part of the complex permittivity and the (b) equivalent conductivity. The relative error is computed with respect to the average across all the samples. The measurements are conducted with “EPCOS TDK N87” at 25 °C. The peak electric field is maintained below 0.05 V/mm.

where  $S_{\text{sum}}$  is the sum of the complex power harmonics and  $E_{\text{rms}}$  the RMS value of the electric field. It should be noted that the measured waveforms are quasi-sinusoidal and, therefore, the harmonic distortion has a negligible impact on the extracted material properties.

Fig. 6 shows the linearized large-signal properties for different frequencies and amplitudes. The electric material behavior is only slightly nonlinear, especially when compared to the massive non-linearities observed for the magnetic properties [4]. The largest nonlinearity can be observed at 400 kHz where the real permittivity and the equivalent conductivity increases by 10 % and 18 %, respectively. The increase of the conductivity with the amplitude is consistent with the microscopic conduction model presented in [14].

#### D. Measurement Repeatability

In order to highlight the variability of the material properties between samples and the consistency of the ferrite electrode contacts, ten different “EPCOS TDK N87” rectangular samples (“I14/1.5/5”) are considered. Five samples feature an electrode

area of 21.0 mm<sup>2</sup> and an electrode distance of 5.0 mm. Five samples feature an electrode area of 70.0 mm<sup>2</sup> and an electrode distance of 1.5 mm.

The small-signal impedance of the different samples is measured and the electrical material properties are extracted. Fig. 7 shows the relative error between the different samples with respect to the average across all the samples. The maximum relative error between the samples is below 10 %, showing that the measurements can be successfully repeated.

Nevertheless, a comprehensive assessment of the sample to sample variation would require the measurement of several sample sizes belonging to different production batches, which is outside the scope of this paper.

### III. IMPACT OF THE DIELECTRIC PROPERTIES

For assessing the impact of the dielectric effects in magnetic circuits, an infinitely long cylindrical core with a sinusoidal magnetic flux is considered (see Fig. 1). At low frequencies, the magnetic flux density is homogeneous and the electric field can be computed with Faraday’s law of induction:

$$|\hat{B}(\rho)| = \hat{B}_{\text{src}}, \quad (9)$$

$$|\hat{E}(\rho)| = \frac{(2\pi f)(\pi\rho^2)\hat{B}_{\text{src}}}{2\pi\rho} = \pi\rho f\hat{B}_{\text{src}}, \quad (10)$$

where  $f$  is the frequency,  $\rho$  the radial distance, and  $\hat{B}_{\text{src}}$  the imposed peak flux density. The spatial RMS value of the fields can be computed as

$$\hat{B}_{\text{int}} = \sqrt{\frac{1}{A} \iint |\hat{B}(\rho)|^2 dA}, \quad (11)$$

$$\hat{E}_{\text{int}} = \sqrt{\frac{1}{A} \iint |\hat{E}(\rho)|^2 dA}. \quad (12)$$

It should be noted that (9) and (10) are only accurate when the dimensional effects are small enough that the flux density is approximately uniform (see Fig. 1). Fig. 8 shows that, for typical applications, the induced electric field is in the range of [0.1 – 1.5] V/mm, which corresponds to the values measured in Fig. 5 and Fig. 6.

#### A. Wavelength and Penetration Depth

The presence of dimensional effects in a ferrite core is usually assessed by computing the complex wavenumber. The wavelength  $\lambda$  and the penetration depth  $\delta$  are the parameters describing the resonances and the skin effect and can be computed as

$$k = 2\pi f \sqrt{\varepsilon_0 \varepsilon_r \mu_0 \mu_r} = \frac{2\pi}{\lambda} - j \frac{1}{\delta}, \quad (13)$$

where  $f$  is the frequency,  $\varepsilon_r$  the complex permittivity, and  $\mu_r$  the complex permeability. Usually, the wave propagation parameters are computed from the small-signal permeability and permittivity [9], [11].

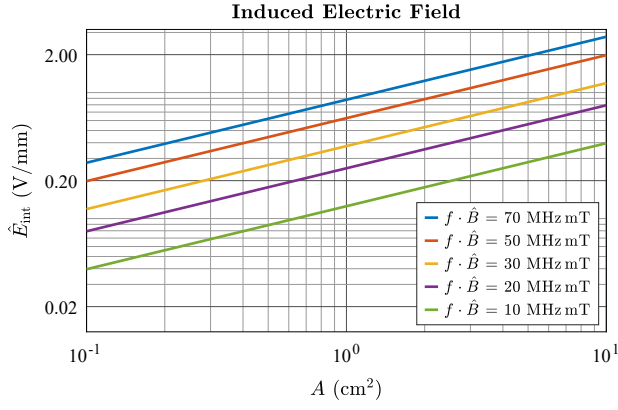


Fig. 8. Induced electric field in a cylindrical core for different flux densities, frequencies, and cross-sections. The quasi-static approximation is used (see (10)) and the spatial RMS value is computed (see (12)).

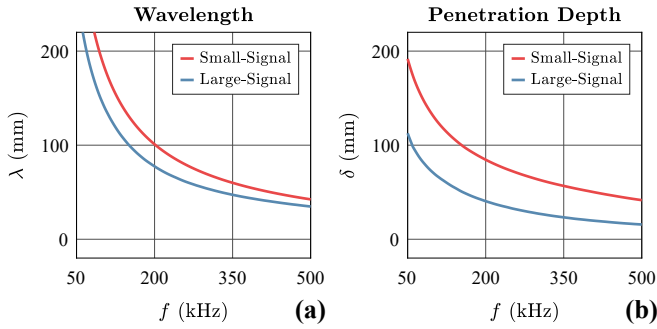


Fig. 9. (a) Wavelength and (b) penetration depth computed for a “EPCOS TDK N87” cylindrical core ( $A = 5 \text{ cm}^2$ ,  $\hat{B}_{\text{src}} = 100 \text{ mT}$ , and  $T = 25^\circ \text{C}$ ). The spatial RMS values (see (11) and (12)) and the quasi-static approximation (see (9) and (10)) are used for evaluating the large-signal material parameters.

Fig. 9 compares the complex wavenumber for small-signal and linearized large-signal material parameters ( $A = 5 \text{ cm}^2$  and  $\hat{B}_{\text{src}} = 100 \text{ mT}$ ). The large-signal permeability is extracted from the MagNet dataset (local linearization) [3], [25]. The large-signal permittivity is taken from Fig. 6. The large-signal (amplitude-dependent) material parameters are evaluated with the spatial RMS values (see (11) and (12)) and the quasi-static approximation (see (9) and (10)).

The impact of the large-signal parameters is non-negligible as it shifts the inception of dimensional effects towards lower frequencies. As the permittivity is almost linear (see Fig. 6), most of the large-signal impact is coming from the permeability [4]. This is particularly important for the penetration depth as the small-signal permeability massively underestimates the magnetic losses [3], [22].

### B. Losses and Reactive Power

Even if the wavelength and penetration depth are useful to assess the presence of dimensional effects, these parameters are not directly relatable to the typical design parameters of power magnetics. For this reason, in this section, the impact of the dielectric effects on the loss and reactive power densities is examined.

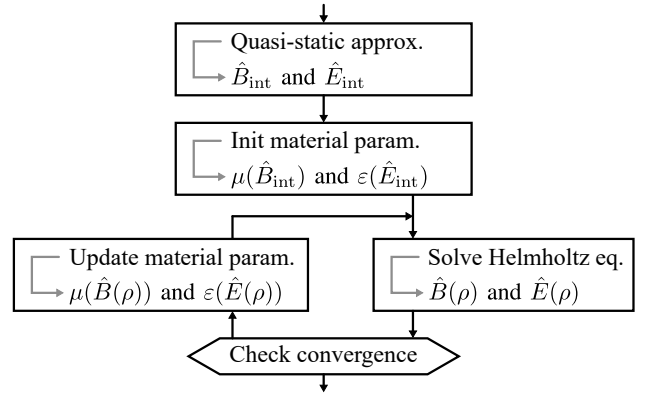


Fig. 10. Iterative process used to solve the Helmholtz wave equation with field-dependent material parameters.

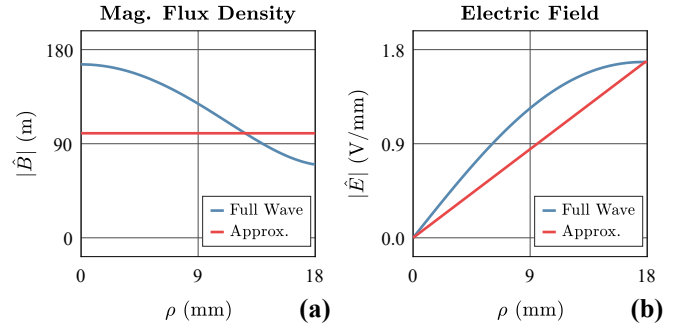


Fig. 11. Radial distribution of the (a) magnetic flux density and the (b) induced electric field density computed for a “EPCOS TDK N87” cylindrical core ( $A = 10 \text{ cm}^2$ ,  $f = 300 \text{ kHz}$ ,  $\hat{B}_{\text{src}} = 100 \text{ mT}$ , and  $T = 25^\circ \text{C}$ ).

At low frequencies, the quasi-static approximation shown in (9) and (10) can be used to compute the electric field. This approximation holds as long as

$$2r < \delta \quad \wedge \quad 2r < \lambda/4, \quad (14)$$

where  $r$  is the radius of the core,  $\delta$  the penetration depth, and  $\lambda$  the wavelength (see (13)). For the quasi-static model, the spatial RMS values (see (11) and (12)) are used to evaluate the linearized large-signal material parameters.

At higher frequencies, the full Maxwell equations should be solved. The Helmholtz wave equation is expressed with the electric field as

$$\nabla^2 \vec{E} = -k^2 \vec{E}, \quad (15)$$

$$\nabla \times \vec{E} = -j2\pi f \vec{B}, \quad (16)$$

where  $k$  is the complex wavenumber (see (13)). The excitation is set in order to impose the following magnetic flux:

$$\left| \iint \vec{B} \cdot d\vec{A} \right| = \hat{B}_{\text{src}} A, \quad (17)$$



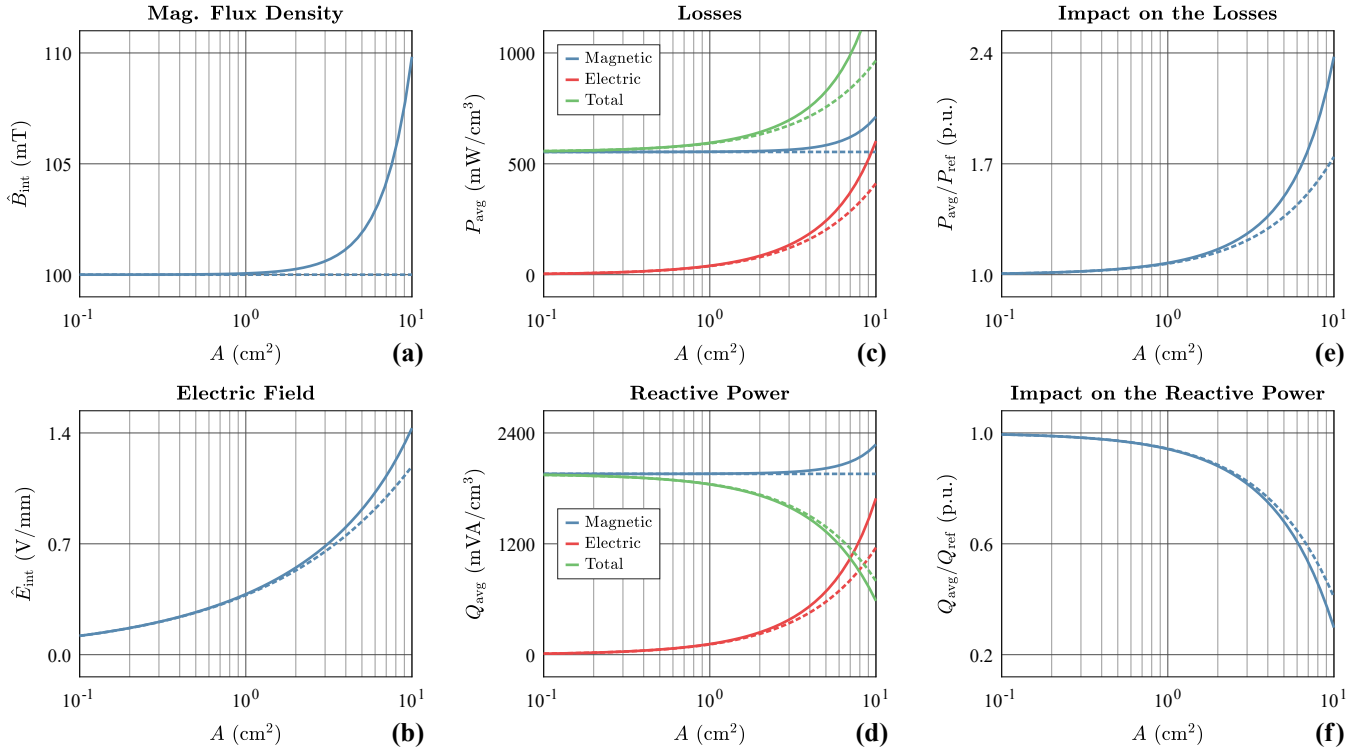


Fig. 12. (a) Magnetic flux density, (b) induced electric field, (c) average loss density, (d) average reactive power density, (e) impact of the dielectric effects on the loss density, and (f) impact of the dielectric effects on the reactive power density. ‘EPCOS TDK N87’ cylindrical cores ( $f = 300$  kHz,  $\hat{B}_{\text{src}} = 100$  mT, and  $T = 25^\circ\text{C}$ ) with different cross-sections are considered. The solid and dotted lines represent the results obtained with the full wave model and the quasi-static approximation, respectively.

where  $A$  is the cross-section and  $\hat{B}_{\text{src}}$  the imposed average peak flux density. This integral condition can be expressed as a boundary condition on the electric field:

$$\hat{E}_{\text{bnd}} = \frac{(2\pi f)(\pi r^2)\hat{B}_{\text{src}}}{2\pi r} = \pi r f \hat{B}_{\text{src}}, \quad (18)$$

where  $r$  is the radius of the core. The partial differential equation is solved in cylindrical coordinates with spatially dependent material parameters. Fig. 10 describes the iterative process used to solve the wave equation with large-signal material parameters.

Fig. 11 shows the magnetic flux distribution and the induced electric field obtained with the quasi-static approximation and the full wave solution ( $A = 10\text{ cm}^2$ ,  $f = 300$  kHz, and  $\hat{B}_{\text{src}} = 100$  mT). With the fully coupled model, the flux distribution is not homogeneous across the cross-section. The spatial RMS values of the fields (see (11) and (12)) are higher with the full wave solution, which indicates that the quasi-static approximation underestimates the active and reactive power levels.

The electric and magnetic complex power densities can be computed from the obtained magnetic flux density and electric field with the material parameters:

$$S_{\text{mag}}(\rho) = \frac{1}{2}(2\pi f) \frac{1}{\mu_0(\mu_r''(\rho) - j\mu_r'(\rho))} \left| \hat{B}(\rho) \right|^2, \quad (19)$$

$$S_{\text{ele}}(\rho) = \frac{1}{2}(2\pi f) \varepsilon_0(\varepsilon_r''(\rho) - j\varepsilon_r'(\rho)) \left| \hat{E}(\rho) \right|^2. \quad (20)$$

In order to get a scalar figure of merit for the active and reactive power levels in the core, the average complex power densities can be computed over the cross-section as

$$S_{\text{avg}} = P_{\text{avg}} + jQ_{\text{avg}} = \frac{1}{A} \iint S(\rho) dA. \quad (21)$$

The impact of the dielectric effects is assessed by comparing the obtained values with respect to the complex power without dielectric effects:

$$S_{\text{ref}} = \frac{1}{2}(2\pi f) \frac{1}{\mu_0(\mu_r''(\hat{B}_{\text{src}}) - j\mu_r'(\hat{B}_{\text{src}}))} \hat{B}_{\text{src}}^2. \quad (22)$$

Fig. 12 shows the quasi-static approximation and the full wave solution for cylindrical cores with different cross-sections ( $f = 300$  kHz and  $\hat{B}_{\text{src}} = 100$  mT). Figs. 12(a)-(b) depicts the spatial RMS values of the magnetic flux density and induced electric field (see (11) and (12)). Figs. 12(c)-(d) shows the average value of loss and reactive power densities (see (21)). Figs. 12(e)-(f) highlights the ratios between the total (magnetic and electric) power and the power obtained without dielectric effects (see (22)). For large cross-sections, the dielectric effects have a significant impact on the field distribution and the power levels. The dielectric effects are increasing the loss density

and reducing the reactive power density as the electric and magnetic reactive powers have opposite signs. The variation of the complex power is also reflected on the impedance of the magnetic circuit (measured between the winging terminals). The real part of the complex impedance is increasing and the imaginary part is decreasing, contributing to a reduction of the quality factor.

For a core with a cross-section of  $3.0 \text{ cm}^2$ , the quasi-static approximation is valid (less than 5 % error). The total loss and reactive power densities are  $1.26\times$  and  $0.82\times$  the values without the dielectric effects, respectively. This highlights that the dielectric effects are already significant in the absence of dimensional resonances.

For a core with a cross-section of  $10.0 \text{ cm}^2$ , the quasi-static approximation is inaccurate (more than 35 % error, see Fig. 11). The total loss and reactive power densities are  $2.38\times$  and  $0.30\times$  the values without the dielectric effects, respectively. Hence, the dimensional resonances massively increase the losses and reduce the impedance of the magnetic circuit.

#### IV. CONCLUSION

This paper analyzes the dielectric properties of MnZn ferrites (“EPCOS TDK N87”) with small-signal and large-signal excitations. The material conductivity increases with the frequency and the temperature. Moreover, it is found that the permittivity and the conductivity only slightly increase with the electric field amplitude, indicating that the dielectric properties are almost linear.

The impact of the dielectric effects on the performance of magnetic circuits is also examined. With large-signal models, the calculated wavelength and penetration depth are significantly lower than predicted by small-signal models. This implies that small-signal models underestimate the inception frequency of dimensional resonances. The magnetic circuits affected by dimensional resonances become extremely lossy (more than 100 % additional losses) and exhibit reduced impedances. Finally, it is found that, below the inception of the dimensional resonances, the dielectric effects can already have a significant impact on the losses (up to 25 % additional losses).

#### ACKNOWLEDGEMENTS

This material is based upon work supported by the National Science Foundation under Grant No. 2242514 (Research Experiences for Undergraduates).

#### DATASETS AND CODE

The “EPCOS TDK N87” permeability and permittivity datasets (small-signal and large-signal) used in this paper are available for download in [15], [16]. The datasets are provided in two different formats: CSV files and MATLAB MAT files. Additionally, the MATLAB source code used for computing the dimensional effects in cylindrical cores (quasi-static approximation and full wave solution) is also available under an open-source license [15], [16].

#### REFERENCES

- [1] A. Goldman, *Modern Ferrite Technology*. Springer, 2006.
- [2] J. B. Goodenough, “Summary of Losses in Magnetic Materials,” *IEEE Trans. Magn.*, vol. 38, no. 5, pp. 3398–3408, 2002.
- [3] H. Li, D. Serrano, T. Guillod, E. Dogariu, A. Nadler, S. Wang, M. Luo, V. Bansal, Y. Chen, C. R. Sullivan, and M. Chen, “MagNet: An Open-Source Database for Data-Driven Magnetic Core Loss Modeling,” in *Proc. of the IEEE Applied Power Electronics Conf. and Expo. (APEC)*, 2022.
- [4] D. Serrano, H. Li, S. Wang, T. Guillod, M. Luo, V. Bansal, N. K. Jha, Y. Chen, C. R. Sullivan, and M. Chen, “Why MagNet: Quantifying the Complexity of Modeling Power Magnetic Material Characteristics,” *IEEE Trans. Power Electron.*, vol. 38, no. 11, 2023.
- [5] E. C. Snelling, *Soft Ferrites: Properties and Applications*. Iliffe Books, 1969.
- [6] F. G. Brockman, P. H. Dowling, and W. G. Steneck, “Dimensional Effects Resulting from a High Dielectric Constant Found in a Ferromagnetic Ferrite,” *Phys. Rev.*, vol. 77, pp. 85–93, 1950.
- [7] G. R. Skutt, “High-Frequency Dimensional Effects in Ferrite-Core Magnetic Devices,” Ph.D. dissertation, Virginia Tech, 1996.
- [8] T. Dimier and J. Biela, “Non-Linear Material Model of Ferrite to Calculate Core Losses With Full Frequency and Excitation Scaling,” *IEEE Trans. Magn.*, vol. 59, no. 7, pp. 1–10, 2023.
- [9] M. Kaćki, M. S. Rylko, J. G. Hayes, and C. R. Sullivan, “Analysis and Experimental Investigation of High-Frequency Magnetic Flux Distribution in Mn-Zn Ferrite Cores,” *IEEE Trans. Power Electron.*, vol. 38, no. 1, 2023.
- [10] S. Dobák, C. Beatrice, V. Tsakaloudi, and F. Fiorillo, “Magnetic Losses in Soft Ferrites,” *Magnetochemistry*, vol. 8, no. 6, 2022.
- [11] G. Skutt and F. Lee, “Characterization of Dimensional Effects in Ferrite-Core Magnetic Devices,” in *Proc. of the IEEE Power Electronics Specialists Conf. (PESC)*, 1996.
- [12] M. Kaćki, M. S. Rylko, J. G. Hayes, and C. R. Sullivan, “Measurement Methods for High-Frequency Characterizations of Permeability, Permittivity, and Core Loss of Mn-Zn Ferrite Cores,” *IEEE Trans. Power Electron.*, vol. 37, no. 12, 2022.
- [13] T. Dimier and J. Biela, “Semi-Analytical Non-Linear Physical Model of Core Losses in Ferrite Ring Cores,” *IEEE Trans. Magn.*, vol. Early Access, 2023.
- [14] W. A. Roshen, “Non-Linear Tunneling Charge Transport in Soft Ferrites,” *Journal of Magnetism and Magnetic Materials*, vol. 312, no. 2, pp. 245–251, 2007.
- [15] T. Guillod, “Large-Signal Properties in MnZn Ferrites: Code and Data,” 2023. [Online]. Available: <https://doi.org/10.5281/zenodo.10059533>
- [16] T. Guillod, “Large-Signal Properties in MnZn Ferrites: Code and Data,” 2023. [Online]. Available: [https://github.com/otvam/large\\_signal\\_ferrite\\_apec24](https://github.com/otvam/large_signal_ferrite_apec24)
- [17] PELCO, “Colloidal Silver, Product Numbers. 16031, 16034,” 2009. [Online]. Available: <https://tedpella.com>
- [18] MG Chemicals, “Silver Conductive Epoxy 8331D,” 2021. [Online]. Available: <https://mgchemicals.com>
- [19] Anatech, “Hummer 6.2 Sputter Coater,” 2020. [Online]. Available: <https://anatechusa.com>
- [20] D. Neumayr, D. Bortis, J. W. Kolar, S. Hoffmann, and E. Hoene, “Origin and Quantification of Increased Core Loss in MnZn Ferrite Plates of a Multi-Gap Inductor,” *CPSS Transactions on Power Electronics and Applications*, vol. 4, no. 1, 2019.
- [21] R. J. Willey, “Humidity and resistivity of MnZn ferrites,” *Journal of Magnetism and Magnetic Materials*, vol. 26, no. 1, 1982.
- [22] TDK / EPCOS, “SIFERRIT Material N87, Datasheet,” 2021. [Online]. Available: <https://tdk-electronics.tdk.com>
- [23] Agilent Technologies, “Agilent 4294A Precision Impedance Analyzer, Operation Manual,” 2003.
- [24] Voltech, “PM6000, Power Analyzer, User Manual,” 2011.
- [25] Princeton University, Dartmouth College, and Plexim GmbH, “MagNet: Data Driven Methods for Magnetic Core Loss Modeling,” 2023. [Online]. Available: <https://mag-net.princeton.edu>